PNAS
RESEARCH ARTICLE | MICROBIOLOGY

Structural basis for the synergetic neutralization of hepatitis E virus by antibody–antibody interaction

Minghua Zheng[a,b,1], Lizhi Zhou[a,b,1], Yang Huang[a,b,1], Xiao Zhang[b,2], Zihao Yu[a,b], Chengyu Yang[a,b], Yuanzhi Chen[a,b], Dong Ying[a,b], Hong Wang[a,b], Zhenqin Chen[a,b], Chang Liu[a,b], Zimin Tang[a,b], Siling Wang[a,b], Kaihang Wang[a,b], Kaixiang Yang[a,b], Yanqing Lin[a,b], Tingting Li[a,b], Qingbing Zheng[a,b], Zizheng Zheng[a,b], Jun Zhang[a,b], Hai Yu[a,b,3], Shaowei Li[a,b,3], Ying Gu[a,b,3], and Ningshao Xia[a,b,3]

Affiliations are included on p. 10.

Edited by Xiang-Jin Meng, Virginia Polytechnic Institute and State University, Blacksburg, VA; received May 4, 2024; accepted September 24, 2024

Neutralizing antibodies (nAbs) play a crucial role in virology, antibody drug development, and vaccine research. In this study, we investigated the synergistic effect of two hepatitis E virus (HEV) nAbs, 8H3, and 8C11, which have exhibited enhanced neutralizing activity in a rhesus monkey model. We presented crystal structures of 8H3 Fab alone and a triple complex of 8C11 Fab and 8H3 Fab simultaneously binding to the HEV E2s protein (8C11:E2s:8H3). Through structural analysis, we identified critical binding sites and fully elucidated the binding footprints of nAb 8H3 in the 8C11:E2s:8H3 complex using site-directed mutagenesis, pinpointing Ile 529, Glu 549, Lys 554, and Ser 566 in the E2s domain, and K66H, S67H, D88H in the 8C11 heavy chain. Interestingly, the synergetic enhancement of 8C11 to 8H3 converted to an antagonistic effect when 8C11 bound to E2s with pretreatment of 8H3, indicating a unidirectional synergistic effect associated with the sequence of antibody involvement. We demonstrated this phenomenon through structural comparisons of E2s:8C11 vs. 8C11:E2s:8H3 crystal structures and molecular dynamics simulations, found that Ile 529 played a key role in the synergistic interplay between these two nAbs. The two-antibody combination showed a more potent antibody-imposed physical disruption mechanism and enhanced coneutralization in an authentic HEV-based cell model. Our study suggests a strategy for synergistic antibody cocktail design with antibody–antibody side-by-side interaction.

hepatitis E virus | neutralizing antibody | immune complex structure | synergetic action

Hepatitis E virus (HEV) is a major causative agent of acute hepatitis in humans, predominantly transmitted through the fecal-oral route. Although traditionally endemic in many developing countries, an increasing number of cases are now reported in developed regions, raising significant health concerns. Particularly alarming is the virus's impact on pregnant women, among whom mortality rates can soar to a critical 20% (1–3). To date, the majority of reports of chronic HEV infection have been associated with genotypes 3 and 4. There is only one report of HEV infection in humans caused by genotype 7 (4), certain cases of chronic hepatitis E may evolve into cirrhosis, and the progression is rapid (5–7). Currently, the therapeutic landscape for HEV is limited and largely consists of the non-specific antiviral Ribavirin (8, 9), which achieves viral clearance in approximately 80% of treated cases. However, these treatments are contraindicated during pregnancy due to potential risks to the fetus.

HEV is a quasi-enveloped, positive-sense RNA virus. It exhibits four major genotypes but a single serotype; genotypes 1 and 2 infect only humans, while genotypes 3 and 4 assume a zoonotic nature with extended infectivity to other animals. The virus has a genome of approximately 7.2 kb consisting of a short 5′ noncoding region, three open reading frames, and a short 3′ noncoding region terminated by a stretch of adenosines (10–13). ORF2 is crucial as it encodes the capsid protein (pORF2) that forms the viral capsid through homodimeric subunits. Different coding regions assemble into distinct conformations, amino acids 112 to 606 (p495) form a T = 1 particle, while amino acids 368 to 606 form particles (p239) utilized as the immunogen in the licensed Hepatitis E vaccine, Hecolin. Hecolin contained aluminum-adjuvanted genotype 1 p239 particles and demonstrated an excellent safety profile and long-term protection efficacy against genotype 4 HEV infection and hepatitis E in phase 3 clinical trials (14, 15). It was first licensed in China in 2012 and recently in Bangladesh in 2022. A truncated form of the E2 protein, located within ORF2 (aa394 to 606), can form homodimers and is implicated in cell recognition, initiating infection (16–18). The minimal homodimer domain E2s (aa455 to 602) has been crystallized and resolved at a high-resolution structure (2.0 Å) (16). Additionally, ORF2 encodes a secreted, non-virion-associated antigen ($ORF2^{s}$)

Significance

Understanding the action mechanism of neutralizing antibodies is critical for combating viral infections. This study delineated the crystal structure of the triple complex composed of the hepatitis E virus (HEV) E2s protein, nAb 8C11, and 8H3 Fab, elucidating the structural foundation for unidirectional synergistic neutralization against HEV through antibody–antibody interaction. It also pinpointed the crucial interacting residues within the 8C11 and 8H3 epitopes, as well as the key sites contributing to the synergism on the 8H3 epitope. The optimal dosage of the two-antibody combination could be estimated by titration curves obtained from appropriate cell or animal models. These findings suggest a strategy to develop combinatorial superantibodies for disease treatment, potentially leading to more effective therapeutic drugs.

The authors declare no competing interest.

This article is a PNAS Direct Submission.

[1] M.Z., L.Z., and Y.H. contributed equally to this work.

[2] Present address: College of Pharmacy, Chongqing Medical University, Chongqing 400016, China.

[3] To whom correspondence may be addressed. Email: yuhai@xmu.edu.cn, shaowei@xmu.edu.cn, guying@xmu.edu.cn, or nsxia@xmu.edu.cn.

This article contains supporting information online at https://www.pnas.org/lookup/suppl/doi:10.1073/pnas.2408585121/-/DCSupplemental.

implicated in the humoral immune escape of HEV, and a diagnostic marker, termed ORF2^u protein, identified in the urine of HEV-infected animals and patients (19, 20).

A number of neutralizing antibodies (nAbs) against HEV have been identified. Among these, 8C11 and 8G12 have demonstrated potent neutralization activities in an HEV disease monkey model and showed high immunodominance in sera from HEV-challenged monkeys and naturally HEV-infected humans. The epitopes of 8C11 and 8G12 have been elucidated by cocrystal structures and show HEV genotype 1 preference and cross-genotype reactivity, respectively, in binding and neutralization assays. Another interesting neutralizing antibody, 8H3, showed lower protection efficacy in the monkey model, but when it was combined with 8C11, it could completely protect animals from HEV challenge, and its binding affinity to E2 protein was enhanced by a 2-log increase. However, the binding footprint of 8H3 and the underlying synergistic effect with 8C11 at the molecular level remain elusive due to its lower affinity for stable immune complex formation (21–23).

In this study, we identified the epitope of by determining the cocrystal structure of E2s bound to 8C11 Fab and 8H3 Fab. We found that the synergistic action stems from the interaction between 8C11 Fab and 8H3 Fab through three specific residues on the 8C11 heavy chain. Interestingly, the low binding affinity of 8H3, which results in conformational drift, contributes to an inverse antagonism effect, impairing the binding of 8C11 to E2s. Using an HEV-based cell model, we confirmed that the two antibodies act synergistically to neutralize the virus and estimated an optimal stoichiometric ratio for coneutralization. These findings suggest a strategy to develop combinatorial superantibodies for disease treatment, potentially leading to more effective therapeutic drugs.

Results

Unidirectional Synergistic Effect of nAb 8C11 on 8H3. In terms of the synergistic effect of 8C11 and 8H3 on affinity determination and in vivo HEV protection, which has been well investigated in our previous studies, we sought to elucidate the synergistic mechanism through biochemistry, structural biology, and molecular dynamics (MD). Initially, we performed analytical ultracentrifugation (AUC) to investigate the complex formation with E2 incubated with either 8C11 or 8H3. 8C11 showed strong affinity to E2s with an increase in the sedimentation coefficient for an exclusive peak of the E2:8C11 Fab complex (7.591S) under condition of E2 surplus (2.658S) in the mixture. In contrast, with an excess of the E2 component, the c(s) profile of E2 and 8H3 Fab revealed two additional peaks. One was the immune complex E2:8H3 Fab, which had a larger sedimentation coefficient value (9.636S) than that of E2:8C11 Fab (7.591S). The other peak represented the remaining unbound 8H3 Fab. These findings suggest that E2 and 8H3 Fab have a lower affinity and may interact with each other in a state of association and disassociation, assuming slightly larger apparent S values than those of the individual components E2 and 8H3 Fab (Fig. 1*A*).

Additionally, we utilized ELISA to assess the synergistic effect of nAbs 8C11 and 8H3. The half-maximum effect dilution times (ET50) was set as the criterion. With HEV genotype 1 E2(I) dimer protein coated as the antigen and preincubated with 8C11, the ET50 value (33,469) demonstrated that 8H3 had nearly an order of magnitude higher binding activity compared to the control (3,033). In contrast, when E2(I) dimer was preincubated with 8H3, the binding affinity of 8C11 decreased by 3.2-fold (Fig. 1*B*). We observed a similar phenomenon with HEV genotype 4 E2(IV), where the enhancement of 8C11 to 8H3:E2(IV) was more than 30-fold, and 8H3 exhibited an 11.3-fold decrease in 8C11 binding affinity to E2(IV) (*SI Appendix*, Fig. S1). These results support that 8C11 has a unidirectional synergistic effect on 8H3 during the binding process of E2(I) and E2(IV) dimer.

We performed a particle disruption test by incubating 8C11 Fab, 8H3 Fab, or their combination either simultaneously for 2 h or by pretreatment of 8C11 Fab for 1 h followed by the subsequent addition of 8H3 Fab for an additional hour (Fig. 1*C*). The samples were prepared as follows: 8C11 Fab to p495 at a molar ratio of 1:1, 8H3 Fab to p495 at a molar ratio of 1:1, 8H3 Fab and 8C11 Fab to p495 at 0.5:0.5:1 simultaneously, and 8C11 Fab to p495 at 1:1 for 1 h followed by 8H3 Fab. The same volume of various samples was analyzed through a GFC column G5000 in High-Performance Liquid Chromatography (HPLC). After incubation of p495 with 8H3 Fab, no complex formed and p495 appeared undisturbed, likely due to the lower affinity and absence of potential clashes with adjacent E2s domains in p495 VLPs. In contrast, when mixed with 8C11 Fab, few p495 particles remained visible in the Electron Microscopy (EM) view, suggesting particle disruption upon 8C11 binding, as has been well characterized in our previous study (24). Similarly, few particles were observed for p495 mixed with both 8C11 and 8H3 simultaneously, but nearly no p495 particles could be found in the EM view in the case of 8H3 addition following 8C11 pretreatment (Fig. 1*C*), which is consistent with the quantified results as decreasing numbers of observed p495 VLPs in the sequence of samples, i.e., p495+8H3 Fab, p495+8C11 Fab+8H3 Fab for 2 h, p495+8C11 Fab for 1 h +8H3 Fab (Fig. 1*D* and *SI Appendix*, Fig. S2). Together, 8C11 and 8H3 also showed unidirectional synergistic effect on triggering the physical disruption of HEV p495 VLPs.

Crystal Structures of 8H3 Alone and Its Complex with E2s:8C11. To elucidate the molecular mechanism underlying the unidirectional synergistic of 8C11 and 8H3, we prepared the 8H3 Fab fragment and E2s(I) in complex with 8H3 and 8C11 Fabs (*SI Appendix*, Fig. S3) and determined the crystal structures of 8H3 Fab alone and the triple-complex at resolution of 1.97 Å and 3.5 Å, respectively (*SI Appendix*, Table S1). The asymmetric unit of the immune complex contains one dimer of E2s bound to two 8C11 Fabs and two 8H3 Fabs (Fig. 2*A*). As previously reported, 8C11 binds to the opposite side of E2s dimerization interface (22), while 8H3 Fab is located on top of the region, with its epitope spanning two E2s subunits (Fig. 2*B*). The interaction between E2s and 8H3 Fab buries a total area of 890 $Å^2$ area, with the heavy chain playing a dominant role and occupying approximately 79.3% (~716 $Å^2$) of the total buried surface area on E2s(I) (Fig. 2*C*). The interaction is primarily polar in character, formed by multiple hydrogen bonds and electrostatic interactions (Fig. 2 *D*–*G*). The heavy chain of 8C11 interacts with the light chain of 8H3, providing an additional contact area of 299.4 $Å^2$. On the interaction surface, contacts within 3 Å include two hydrogen bonds (Ala64^{8C11}-Asn82^{8H3}, Ser67^{8C11}-Asn82^{8H3}), two salt-bridges (Lys66^{8C11}-Asp66^{8H3}, Asp88^{8C11}-Lys18^{8H3}) and a strong van der Waals interaction (Arg68^{8C11}-Asn82^{8H3}), all located between the framework regions of the two antibodies (Fig. 2*H*). In conclusion, the binding of 8H3 to E2s is structurally stabilized by numerous hydrogen bonds, van der Waals forces, and electrostatic interactions, and is further supported by 8C11.

Pivotal Sites at 8C11:8H3 Interface Responsible for Synergistic Neutralization by 8C11 to 8H3. In our previous study, we reported the crystal structure (PDB ID: 3RKD) of nAb 8C11 in complex with E2s (I) at a 2:1 Fab to E2s dimer molar ratio. Superposition of the E2s:8C11 Fab complex onto the E2s:8H3 Fab:8C11 Fab complex, aligned by the E2s structure, revealed an additional

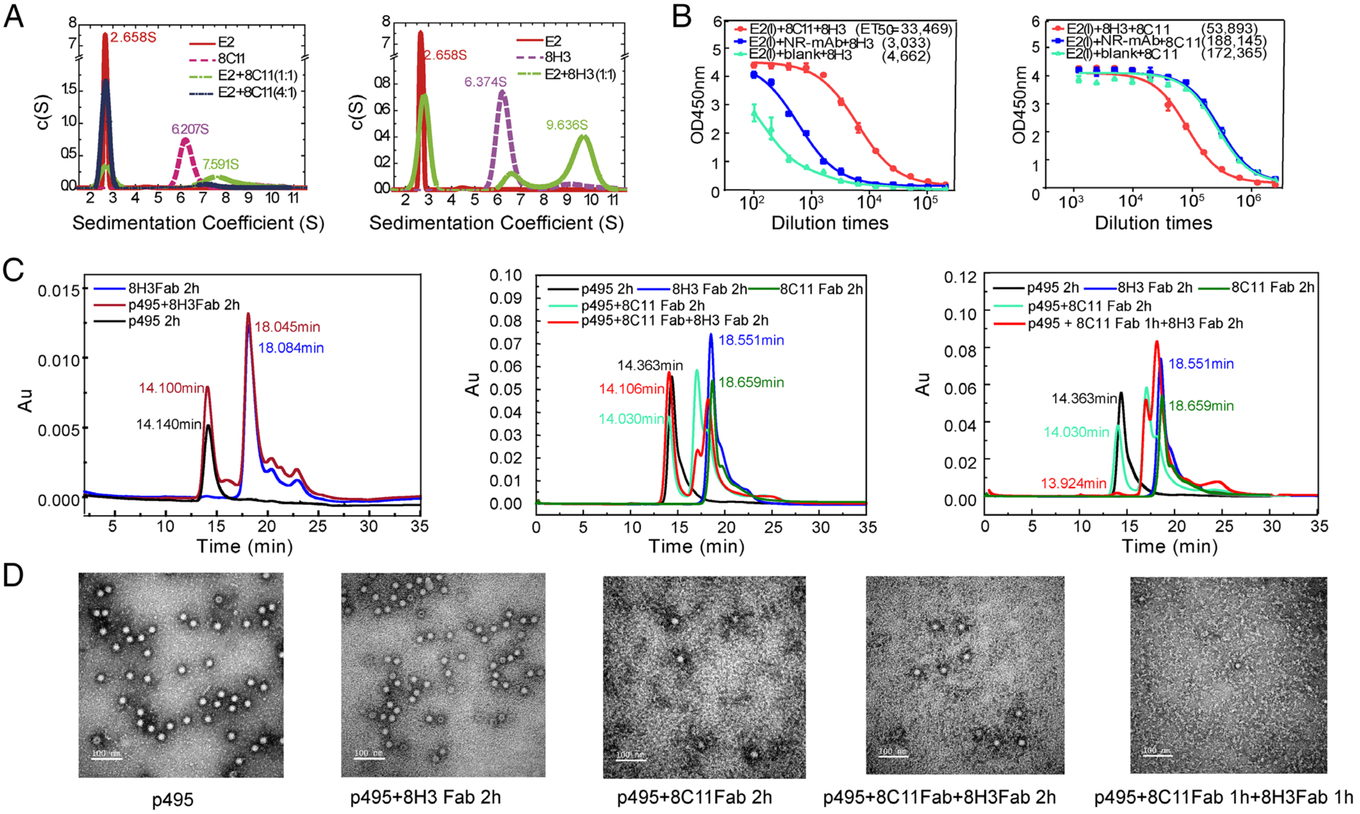

Fig. 1. Synergistic effect on 8H3's binding activity and VLP disruption with the pretreatment of nAb 8C11. (*A*) SV analysis of mAb 8C11 and 8H3 binding to E2, revealing partial dissociation of 8H3 from E2 due to weak affinity. (*B*) Unidirectional synergistic action of nAbs 8C11 and 8H3 evaluated using an indirect ELISA with purified E2 protein-coated plates. ET50 stands for half-maximum effect dilution fold. *Left* panel: E2(I) plates reacted with 8C11 or no 8C11 Fabs, followed by 8H3-HRP, showing corresponding binding curves. Red line represents E2s(I) + mAb 8C11 + mAb 8H3, ET50 = 33,469. Blue line represents E2s(I) + nonrelated mAb (anti-HPV mAb A12A3) + mAb 8H3, ET50 = 3,033. Green line represents E2s(I) + mAb 8H3, ET50 = 4,662. *Right* panel: E2(I) plates reacted with 8H3 or no 8H3 Fabs, followed by 8C11. Red line is E2s(I) + mAb 8H3 + mAb 8C11, ET50 = 53,893. Blue line is E2s(I) + nonrelated mAb + 8C11, ET50 = 188,145. Green line represents E2s(I) + mAb 8C11, ET50 = 172,365. (*C*) HPLC-G5000. *Left*: black, p495. Blue, 8H3 Fab. Red p495+8H3 Fab, equally 8H3 Fab loading amount. *Middle*: Black, p495. Blue, 8H3 Fab. Dark green, 8C11 Fab. Light green, p495 + 8C11Fab 2 h. Red, p495+8C11 Fab+8H3 Fab 2 h, equally loading p495 amount. *Right*: Black, p495. Blue, 8H3 Fab. Dark green, 8C11 Fab. Light green, p495 + 8C11Fab 2 h. Red, p495+8C11 Fab 1 h+8H3 Fab 1 h. equally loading p495 amount. (*D*) TEM data. HEV-p495 VLP (495), p495+8H3 Fab incubate 2 h, 495:8C11 Fab incubated for 2 h, p495:8C11 Fab:8H3 Fab incubated for 2 h. p495 and 8C11 Fab incubate for 1 h followed with 8H3 Fab for 1 h. incubate in 37 °C.

Ab–Ab interaction causing a 6.3° shift in 8C11's original binding orientation (Fig. 3*A* and Movie S1), indicating a collision between 8H3 Fab and 8C11 Fab. Five pairs of amino acids located on the interface were considered to dominate this interaction (Fig. 2*F*). To determine whether the Ab–Ab interaction consolidates the binding of 8H3 binding to E2s, leading to synergistic enhancement, we generated a series of 8C11 mutants, including K66A, S67A, R68A, and D88A. As shown in Fig. 3*B*, 8C11 mutants K66A, S67A, and D88A maintained high reactivity to E2 except R68A which significantly attenuated reactivity, indicating that R68 is crucial maintaining inherent conformational stability (Fig. 3*B*). While the enhancing ability of 8C11 binding the single-site E2 mutant K66A, S67A, or D88A was the same for wild-type (WT) E2 (Fig. 3*C*). Therefore, we generated a triple amino acid mutant (8C11-KSD, harboring K66A, S67A, and D88A) and found an 18-fold decrease in 8H3 binding activity (Fig. 3 *D* and *E*). These results demonstrated that 8H3 overlaps with 8C11 through K66A, S67A, and D88A to increase the total binding activity of 8H3 to E2. In other words, establishing and maintaining stable 8H3/8C11 interactions is crucial to enhancing the binding ability of 8H3 to E2.

Critical Sites on 8H3 Epitope Involved in 8H3 Binding to E2s and the Antagonism Effect of 8H3 to 8C11. In the E2s:8C11 Fab:8H3 Fab complex structure, 11 amino acids from the E2s (I) domain were observed interacting with 8H3 Fab through their side chains, including I529, T552, T563, T564, Q531, N560, Q568, T553, E549, K554, and S566. Structure-based functional studies on the corresponding E2 mutants were performed to determine the significance of these interactions (Fig. 2 *C* and *E*). The relative effective concentration 50 (rEC50) was calculated as the reciprocal of the EC50 value against the EC50 of E2WT to reflect the variations in mutant antigenicity. Mutants T552A, T563A, and T564A lost the ability to dimerize (Fig. 4*A*) and showed no reactivity against 8H3. According to the rEC50 results, mutants Q531A, N560A, Q568A, and T553A exhibited similar antigenicity as E2 wild type. However, mutants E549A, K554A, and S566A showed significantly decreased binding activity with 8H3 mAb. Intriguingly, the I529A mutation exhibited increased binding activity with 8H3 (Fig. 4*B*), consistent with AUC and western blot experiments, which indicated that the I529A mutant exhibited a higher binding capacity (11.00 S) in solution (Fig. 4 *C* and *D*). Mutants N560A and T553A exhibited similar s values when forming an immune complex with 8H3 (~7.33 S) (*SI Appendix*, Fig. S4), while E549A, T554A, and S566A mutations abrogated the formation ability of the immune complex (Fig. 4 *E*–*G*). These data underscore the pivotal roles of I529, E549, S566, and K554 in the binding of 8H3 to E2s, marking them as essential epitopes for 8H3.

We then investigated the antagonistic effect of 8H3 on the binding of 8C11 to E2s. First, mutants of 11 amino acids on the E2:8H3 binding surface were assessed for their synergistic effect

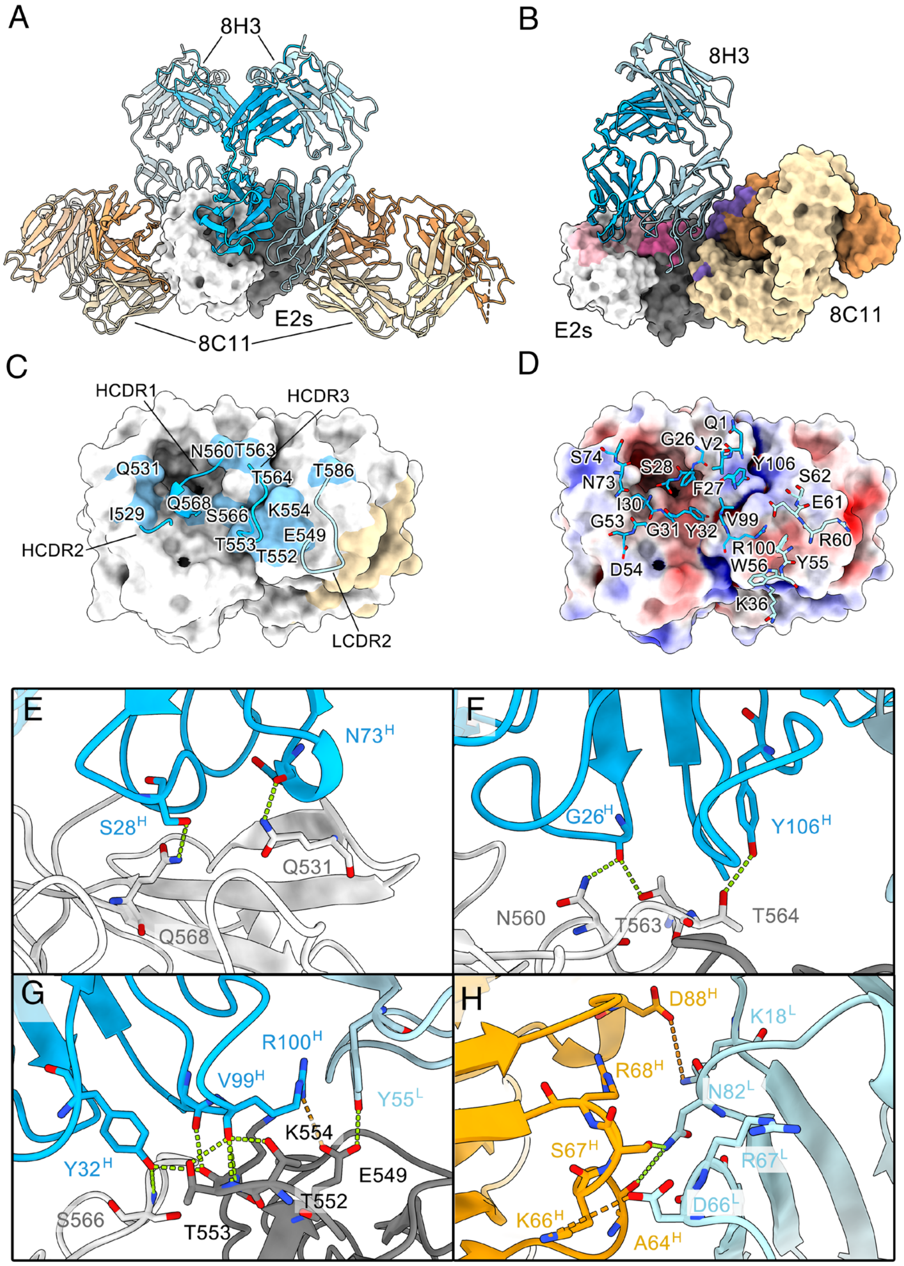

Fig. 2. E2s:8C11 Fab:8H3 Fab complex structure. (*A* and *B*) Structure of an E2s dimer bound to two 8C11 Fabs and two 8H3 Fabs. Interactions between 8C11 Fabs, 8H3 Fabs, and 8C11:8H3 Fabs are colored in faint yellow, magenta, and violet, respectively. (*C*) Surface representation of E2s(I) with interacting epitope residues highlighted in blue for the 8H3 heavy and light chains. (*D*) Electrostatic potential surface of the E2s(I) epitope (red: negative, blue: positive, gray: neutral) with key interacting residues from 8H3 loops 1, 2, 3, and 4 shown as sticks. (*E*–*G*) Hydrogen-bonding and salt bridge contacts between E2s(I) and neutralizing antibody 8H3 (green and yellow dotted lines, respectively). (*H*) Interface-interacting amino acids shown as stick models, including K66, S67, R68, and D88 from 8C11 heavy chain, and D66, N82, and K18 from 8H3 light chain. Interactions including one hydrogen bond (blue), one salt-bridge (orange), electrostatic interactions, and other contacts (lime) are formed between the framework regions of the two antibodies. Epitope regions of 8H3 on different E2 subunits are shown in varying shades of pink.

on binding to 8C11 by ELISA with E2 preincubated with 8C11 before binding with 8H3. Mutations T552A, T563A, and T564A abolished the interaction of E2s with 8H3, thus did not show increased binding activity (*SI Appendix*, Fig. S5). Other eight antigen mutants exhibited a 10-fold increase in synergy compared to E2s-WT (Fig. 5*A*). Notably, the synergistic action of 8C11 to 8H3 in the I529A mutant is overshadowed by its elevated affinity as well as the antagonism effect of 8H3 to 8C11 (Fig. 5*B*).

Unidirectional Synergistic Effect Mechanism Revealed by MD Simulation. We utilized MD simulations to explore the unidirectional synergistic effect mechanism between the nAbs 8C11 and 8H3 against the HEV. The MD simulation of the E2s:8H3 complex, conducted over 200 ns, revealed considerable dynamism and instability in the 8H3 antibody when targeting the E2s domain alone, as indicated by the RMS fluctuation (RMSF) values (*SI Appendix*, Fig. S6). Specifically, 8H3 exhibited significant deviations from its binding regions, and the complementarity-determining region loop lost its original interactions with the E2s domain (Fig. 6*A*), suggesting that 8H3 may have difficulty maintaining stable interactions with the E2s domain. However, the inherent binding instability of 8H3 was substantially mitigated by the presence of 8C11 Fab (Fig. 6*B* and *SI Appendix*, Fig. S6). Given the overlap of 8C11 with the potential deflection trajectory of 8H3, it is postulated that the two loops of 8C11 might help secure 8H3 near its original position,

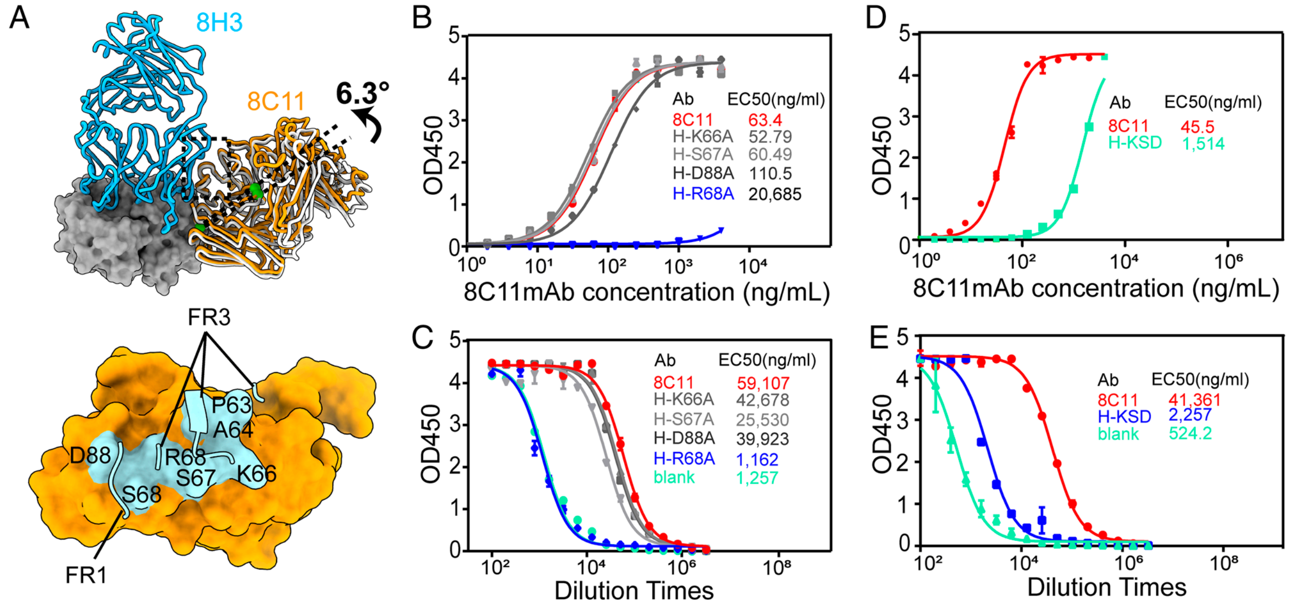

Fig. 3. The synergistic action of 8C11 and 8H3. (*A*) Conformational change of 8C11caused by 8H3. 8H3 Fab colored with cyan, 8C11 Fab in the E2:8C11 Fab:8H3 Fab complexes colored by orange, 8C11 Fab in E2:8C11 Fab colored by silver (top). Surface representation of 8C11 Fab with interacting epitope residues highlighted in cyan for the8H3 Fab heavy and light chains (bottom). (*B*) Reactivity of single-site 8C11mAb mutants against E2 protein tested by ELISA, with EC50 values calculated through sigmoid trend fitting. (*C*) Interaction of single-site 8C11mAb mutants with 8H3 against E2 protein assessed by ELISA, with EC50 values calculated through sigmoid trend fitting. (*D*) Reactivity of three-point mutant against E2 protein tested by ELISA, with EC50 values calculated through sigmoid trend fitting. (*E*) Interaction of three-point mutant 8C11-KSD with 8H3 against E2 protein assessed by ELISA, with EC50 values calculated through sigmoid trend fitting. The letter "H" stands for heavy chain of 8C11 antibody. 8C11 is wild type antibody without mutation.

thereby stabilizing the engagement of 8H3 (Fig. 6*C*). Additionally, the binding free energy, calculated using MMPBSA (Molecular Mechanics Poisson–Boltzmann Surface Area), demonstrated a higher affinity of 8H3 for the 8C11 complex, consistent with experimental observations (*SI Appendix*, Fig. S7). These results suggest that the binding of 8H3 is favored by the preformed E2s:8C11 complex, as indicated by increased stability and affinity.

Subsequent investigations into the negative synergistic effect of 8H3 on 8C11 sought to elucidate its mechanism by examining the structural variability of the E2s domain and the antibody in the simulated E2s:8H3 complex. Comparison of RMSF values from the E2s alone and the E2s:8H3 complex showed no significant variations in the epitope regions of 8C11 (*SI Appendix*, Fig. S8), indicating that 8H3 does not disrupt 8C11's binding by indirectly affecting the conformation of its epitopes. However, it was observed that the conformational drift of 8H3 could lead to the loss of two electrostatic interactions in the cocrystal structure of E2s:8H3:8C11, and the formation of repulsive interactions between Lys66 of the 8C11 heavy chain and Arg60 of the 8H3 light chain (Fig. 6*D*). Given the highly dynamic nature of 8H3 targeting to E2s alone demonstrated in the MD simulation, we propose that the unfavorable contacts between 8H3 and 8C11, caused by the postural drift of the prebound 8H3, underlie the mechanism by which 8H3 unidirectionally weakens the binding affinity of 8C11 to the E2s domain (Fig. 6*D*). To further validate this, the E2s-I529A mutant, which showed elevated affinity for 8H3, was employed in an MD study. Expectedly, the simulation of E2s-I529A:8H3 showed that the unfavorable deviation of 8H3 was markedly reduced compared to that observed in E2s:8H3 (Fig. 6*E*). In the I529A mutation, a smaller nonpolar side chain may enable I30 on the 8H3 heavy chain to insert more deeply into the reshaped hydrophobic groove at the interface, thus enhancing local hydrophobic packing and stabilizing the binding of 8H3 (*SI Appendix*, Fig. S9).

Taken together, the instability and potential deviation of bound 8H3 introduce steric hindrance, diminishing the likelihood of 8C11 Fab binding to E2s and consequently exerting an antagonistic effect (Fig. 6*F*). The I529-I30 pair should be considered a hotspot for therapeutics design.

Synergistic Effect of 8C11 and 8H3 While Capturing Authentic HEV. We compared the synergistic effect of 8C11 and 8G12 on 8H3 using an in vitro virus capturing model. 8G12 is another neutralizing antibody against HEV. Fluorescence quantitative PCR was employed to quantify the captured virus RNA. Native HEV was obtained from the bile of monkeys challenged with HEV. Our results indicated that preincubation with both full-length 8C11 and its Fab fragment effectively enhanced the binding of 8H3 Fab to native HEV. Notably, the full-length 8C11 exhibited a significantly higher enhancement effect than its Fab fragment, suggesting that the bivalent nature of the full-length antibody confers an avidity effect. In contrast, the control antibody 8G12 showed no observable enhancement, likely due to its competition with 8H3 for binding to overlapping epitopes on the E2s domain (Fig. 7*A*). Other nonbinding control antibodies showed no enhancement in 8H3 virus capturing (*SI Appendix*, Fig. S10). Native HEV capturing by 8C11 Fab exhibited a concentration-dependent manner. Additionally, we investigated the synergistic neutralizing effect of 8C11 and 8H3 in native HEV using a cell-based model (Fig. 7*B*). IC50 (Half-maximal inhibitory concentration) and combination index (CI) were analyzed by the Compusyn program to evaluate the synergy of the two Abs (25, 26). The CI value of the mixture at IC50, IC75, IC90, and IC95 were 0.134 µg/mL, 0.150 µg/mL, 0.169 µg/mL, 0.183 µg/mL respectively, all less than 1, which demonstrated a significant synergistic effect in virus neutralization (*SI Appendix*, Fig. S11). Data within linearity range were fitted using simple linear regression, generating a possible optimal dosage of 0.856 µg. The results also suggest the unidirectional synergistic effect of 8C11 on 8H3. As the antibody concentration increases beyond the intersection point of the two dose–response curves (Fig. 7*B*), the synergistic effect of 8C11 on 8H3 reaches its peak and then turns to the antagonistic effect of 8H3 on 8C11.

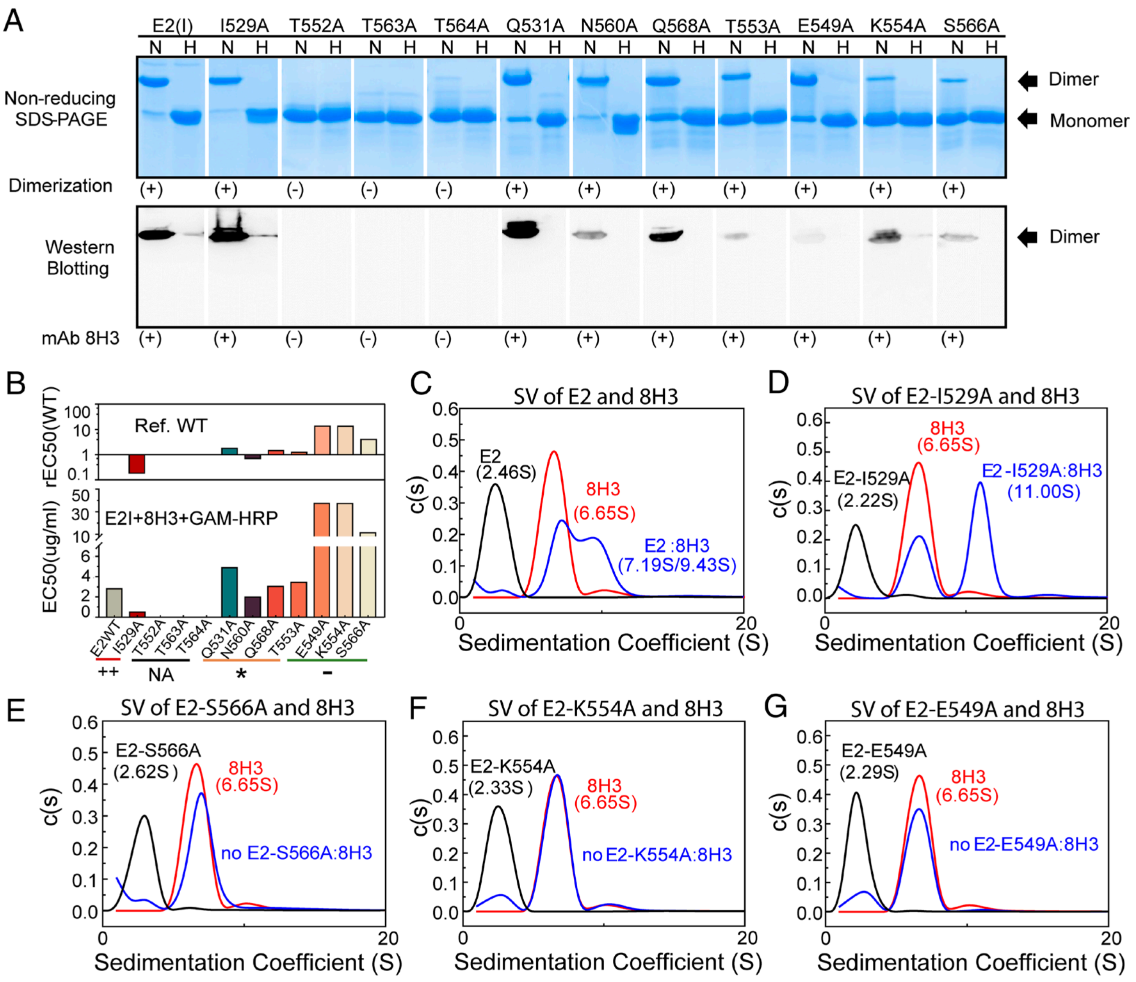

Fig. 4. Mutagenesis on E2s(I):8H3 interaction interface. (*A*) Nonreducing SDS/PAGE and Western blotting with neutralizing mAb 8H3 to evaluate mutation effects onE2s(I):8H3 interaction. Samples heated in reduced (H) or nonreducing (N) conditions. (+): dimerization or reactivity with 8H3, (−): monomer or loss of the respective property. (*B*) Reactivities of E2s dimer or mutants against 8H3 mAbs quantified as EC50 values (*Bottom*) and corresponding rEC50 values (*Upper*). Smaller rEC50 values indicate higher reactivity for E2s dimer against mAbs relative to WT E2s. EC50 values obtained from the mean value of two repeated experiments. (*C*–*G*) SV analysis of mAb 8H3 binding to E2s(I) and mutants I529Ala, E549Ala, K554Ala, and S566Ala in solution. c(s) profiles of E2, E2 mutants, mAb 8H3, and antigen–antibody mixture spotted as black solid lines, red solid lines, and blue solid lines, respectively.

Discussion

In this study, we identified a unidirectional synergistic effect between two nAbs, 8C11 and 8H3, against the HEV. The ORF2 gene encodes the sole HEV capsid protein. This protein, pORF2, comprises 660 amino acids, including an arginine-rich region spanning 110 amino acids at the N terminus, which serves as the primary binding site for HEV genome RNA. The capsid protein, initially encoded as an 82 kDa precursor (ppORF2), undergoes cleavage of its N-terminal signal peptide in the endoplasmic reticulum, resulting in a ~72 kDa mature capsid protein (pORF2). Due to the high hydrophobicity and insolubility of the full-length protein, various truncated forms have been developed as vaccine candidates, including E2 (amino acids 394 to 606, 23 kDa), p239 (amino acids 368 to 606, 30 kDa), T = 1 virus-like particle (VLP) (amino acids 112 to 606, p495), and T = 3 VLP (amino acids 14 to 608, p595). Notably, the E2s domain of the HEV dimer is crucial for binding HEV-nAbs, determining the virus's host tropism and cellular entry mechanisms (27, 28).

We solved the cocrystal structure of the HEV protruding domain E2s (genotype I) in complex with 8C11 Fab and 8H3 Fab, revealing that mAb 8H3 interacts with mAb 8C11 at residues K66, K67, and D88 of the 8C11 heavy chain, in addition to binding at an epitope at E2s, which only creates a relatively weaker interaction than that of 8C11. With the assistance of 8C11 interaction, we identified Ile 529, Glu 549, Lys 554, and Ser 566 as critical sites on the 8H3 epitope. This overlapping configuration enhances the steric binding stability, contributing significantly to the observed synergistic effect. Conversely, any deviation in 8H3 positioning induces steric hindrance, leading to antagonism toward 8C11, thereby establishing a unidirectional synergistic mechanism.

Decades of antibody research have uncovered various interaction types that influence therapeutic efficacy. Recently, a significant number of synergistic nAbs have been discovered across different viruses. For example, a cocktail therapy targeting Coxsackievirus B1 (CVB1) employs three CVB1-specific nAbs that recognize different epitopes within the capsid VP2 protein's highly variable EF loop. This combination perturbs capsid–receptor interactions, achieving synergistic neutralization through a stepwise capsid transition and virion disruption, indicative of dynamic virion changes in response to nAbs targeting the receptor-binding site (29). Another notable synergistic effect was identified against COVID-19, where two antibodies in a single-chain diabody format demonstrated a synergistic effect. This synergy, primarily due to the binding orientation on the receptor-binding domain (RBD)-5, facilitates interspike cross-linking and promotes the exposure of cryptic epitopes, enhancing binding efficacy. In the case of antibodies

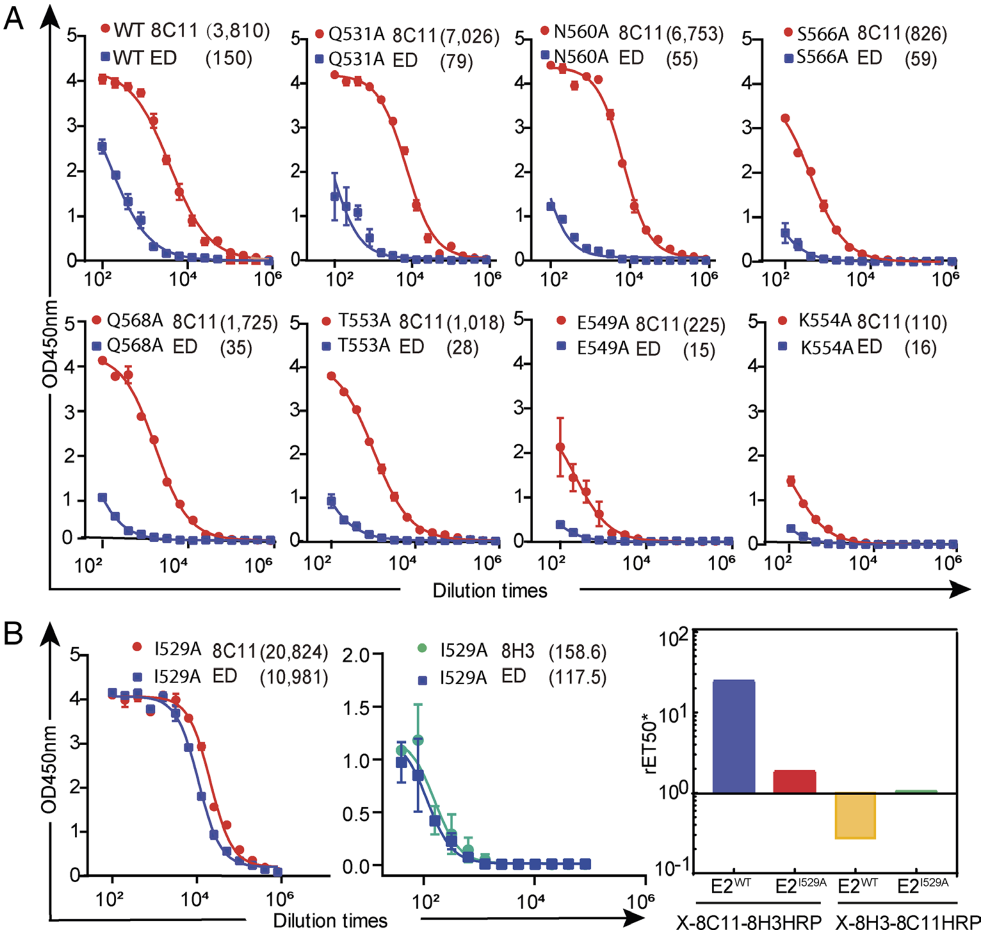

Fig. 5. The E2:8H3 Interface associated with the interaction enhancement of 8C11 and 8H3 mAbs. (*A* and *B*) ELISA-based assessment of interaction enhancement between 8C11 and 8H3 mAbs against mutant E2 proteins, with ET50 values calculated through sigmoid trend fitting. The ET50 values for each curve are shown in parentheses. Blue line represents the control group with E2 mutant-coated plates, ED-blocked E2 incubation, and 8H3-HRP as the secondary antibody (OD450). Red line represents the experimental group with 8C11 as the first antibody against coating E2 mutants, and 8H3-HRP as the second antibody (OD450). Green line represents the experimental group with 8H3 as the first antibody against coating E2 mutants, and 8C11-HRP as the second antibody (OD450). (*B*) *Right* panel summarizes the synergistic fold of E2sWT and E2sI529A. "X" stands for E2 WT and E2I529A.

H014 and H27 against SARS-CoV-2, partial epitope occupancy by H014 facilitates the transition of the RBD from a "closed" to an "open" state, enhancing interaction with H27 in a synergistic manner and yielding a 100-fold increase in binding affinity (30, 31). It is noteworthy that, to date, a unidirectional synergistic effect of antibodies has not been reported in other pathogens, where no difference is observed upon varying the sequence of addition of multiple antibodies. In the present study, the sequential addition allows the first antibody to trigger conformational changes that enhance the secondary antibody's effect, which is nondirectional and distinct from the enhancement of 8C11 to 8H3 by antibody–antibody interaction. Interestingly, 8H3 assumes an antagonistic action upon 8C11 binding. Antibodies with antagonistic mechanisms offer some advantages in therapeutic antibody development, such as PD-1 and PD-L1 (32, 33), widely used in tumor therapy. Thus, the unidirectional antibodies exhibit more complex properties for combinatory antibody design; by binding initially, the first antibody leaves ample space for the second, thereby enhancing overall binding capability. However, if the second antibody binds first, the overall binding effectiveness would be alleviated, suggesting an interesting strategy on tunable efficacy for combinatory antibodies by altering their involvement sequence.

Our findings offer critical insights into the structural basis of the synergistic effect between two nAbs against HEV. This structural information and the elucidated unidirectional mechanism provide valuable insights for developing therapeutic strategies, demonstrating the profound impact of antibody interaction dynamics on drug development.

Materials and Methods

Cloning and Purification. The E2 genes of HEV genotype 1 and 4 were PCR-amplified from human and swine HEV capsid protein gene, respectively (Accession Nos. NC_001434.1 and GQ166778). All mutated constructs, including antibodies and antigens, were generated using site-directed PCRs. The pTO-T7 expression plasmid and E. coliER2566 strain were used for protein expression. HEV E2s(I) was purified according to our previously published study (10). The nAbs used in this study were produced in mouse ascites fluid and affinity purified with a Protein A column. Fab fragments were prepared from purified mouse monoclonal antibodies by papain cleavage and purified by diethylaminoethyl (DEAE). The E2s(I):8C11 Fab:8H3 Fab (ratio of 1:1.5:1.5 M) was incubated at 37 °C for 2 h, purified using TSK Gel G5000 PWXL with HPLC, and concentrated to approximately 8 mg/mL. The ORF2 gene fragment of HEV genotype 1, encoding residues 112 to 606, named p495, was cloned into pFastBac plasmid (Invitrogen). Sf9 cells were transfected by lipofection to produce recombinant viruses. Tn5 cells in ESF 921 were infected with the recombinant baculoviruses for 4 d at 30 °C. The target proteins (p495) were mainly secreted into the culture medium. p495 in the cell culture supernatant was concentrated by incubation with 8% polyethylene glycol 6000 in the presence of 0.4-M NaCl at 4 °C overnight. The precipitate was resuspended in 20-mM phosphate buffer pH 6.0 (PB6.0) and purified using a DEAE-5PW column.

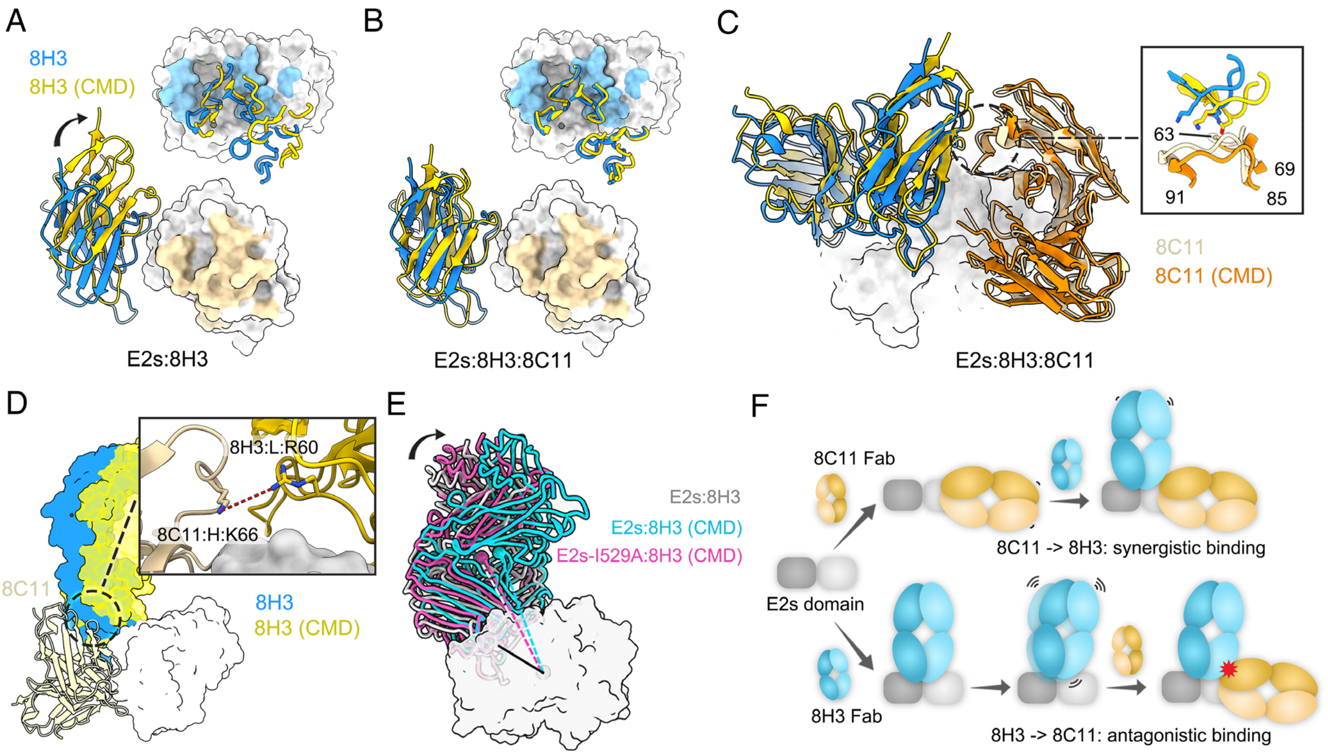

Fig. 6. Unidirectional synergistic effect mechanism revealed by MD simulation. (*A*–*D*). Comparison of the structural features of the simulated E2s:8H3:8C11 (*A* and *D*) and E2s:8H3 complexes (*B* and *C*). 8H3 Fab before and after MD is depicted in blue and yellow cartoons, respectively, while E2s is shown as a white surface. (*A* and *B*) Epitope regions for 8C11 and 8H3 are highlighted in wheat and light blue, respectively. (*C*) 8C11 Fab before and after MD is shown in wheat and orange cartoons, respectively. (*D*) Alignment of 8C11 (wheat) to the simulated E2s:8H3 model using the E2s domain as a reference, revealing poor contact (red dashed line) between positively charged residues (stick) from both Fabs. (*E*) Structural feature comparison of simulated E2s:8H3 (pink) and E2s-I529A:8H3 (blue) complexes. (*F*) Proposed mechanism for the synergistic neutralization mechanism of 8H3 and 8C11 antibodies based on the MD simulation studies. CMD, indicates the models were generated after MD simulation.

Crystallization and Structure Determination. Triple-complex crystals were grown by mixing 1 μL of the E2s(I):8C11 Fab:8H3 Fab complex with 1 μL of reservoir solution (0.2 M $MgSO_4$, 8% glycerol, and 11% PEG 40000) using the hanging-drop vapor diffusion method at 20 °C. Similarly, 8H3 Fab was purified, and crystals were grown from a reservoir solution consisting of 2M Mg(Ac)2 and 18% PEG 3350. A cryoprotectant solution containing 30% glycerol supplemented with reservoir conditions was used for both crystals, and data were collected at 100 K. Datasets were processed using HKL2000, and the structures were solved by molecular replacement with PHASER. Models were built using COOT, refined by Phenix, and analyzed by PROCHECK (*SI Appendix*, Table S1). Molecular visualization programs PyMOL and ChimeraX were used to prepare the figures (24).

Antibodies. Monoclonal antibodies targeting E2(I) and E2(IV) were generated using a standard murine monoclonal antibody preparation protocol (23). A chimeric antibody was expressed in Chinese hamster ovary cells by codon optimizing the mouse monoclonal antibody variable region genes of the heavy and light chains and cloning them into PTT5 vectors containing the constant regions of mouse heavy and light chains, respectively. Paired heavy and light chain expression cassettes were transiently cotransfected into CHO cells, and antibodies were purified from the culture supernatant 7 d posttransfection using a protein-A column.

Sodium Dodecyl Sulfate-Polyacrylamide Gel Electrophoresis (SDS-PAGE). Protein samples were mixed with 2× loading buffer consisting of 100-mM Tris-HCl (pH 6.8),4% SDS, 0.2% bromophenol blue, 200-mM DTT, and 20% glycerol, and were then subjected to 12% gradient SDS-PAGE. Separated proteins were stained with Coomassie Brilliant Blue following standard laboratory protocols.

High-Performance Size-Exclusion Chromatography (HPSEC). Purified HEV E2 protein or complexes were analyzed by HPLC using an Agilent Technologies 1200 series system (Santa Clara, CA) and a TSK Gel G5000 PWXL 7.8 × 300-mm column (TOSOH, Tokyo, Japan). The proteins were eluted at a flow rate of 0.5 mL/min and detected at 280 nm for subsequent analysis or sample preparation.

ELISA for Enhancement Assay. A 96-well microplate was coated with the antigen (200 ng/well) and incubated with serial dilutions of each monoclonal antibody (mAb) at 37 °C for 1 h. After the incubation, the wells were treated with HRP-conjugated 8C11 or 8H3 for 30 min at 37 °C. The tetramethylbenzidine substrate (100 μL) was then added to each well and incubated for 10 min at 37 °C. The reaction was stopped by adding 50 μL of 2 M H2SO4, and the optical density (OD) was measured at 450 nm with a reference wavelength of 620 nm.

AUC. Sedimentationvelocity (SV) was used to monitor the binding of the antigen and monoclonal antibody in a neutral solution. All samples were diluted to approximately 1.0 OD280nm in a 1.2-cm light path with phosphate-buffered saline (PBS; pH 7.4). The rotor speed was set at 50,000 rpm for E2 and its mutants, 40,000 rpm for mAb 8C11 and 8H3, and 30,000 rpm for the immune complex. The sedimentation coefficient was obtained with the c(s) method using Sedfit software provided by P. Schuck (NIH, Bethesda, MD).

Virus Capturing Analysis. HEV from Rhesus monkey stools was prepared in PBS and incubated with serial dilutions of nAbs 8C11, 8C11 Fab, and 8G12 for 30 min at 37 °C. Antibody dose initiated from 1.25 μg. The nAb8H3 (1 μg/well) was coated in a 96-well microplate and incubated with the mixtures of virus–antibody at 37 °C for 1 h. Subsequently, the microplate was washed ten times with PBST, and HEV RNA was purified from 50 μL of each sample. The HEV RNA copy number was determined by quantitative real-time reverse transcription–PCR (RT-PCR) as previously reported (34).

ORF2^S-Based HEV Neutralization Cell Model and Antibody Synergistic Test. HEV genotype 3 stocks were generated by transfecting S10-3 cells with in vitro-transcribed HEV RNA according to Yin et al. (35). Neutralization assays were conducted using virus stock to infect the HepG2/C3A cell line, where the viruses propagated and efficiently expressed ORF2^S in a secretory manner (19). We quantified the ORF2^S proteins in cell culture supernatant using a HEV ELISA Kit (Innovax, InnoDx). The inhibition rate of ORF2^S expression when antibodies prevented virus infection was used to measure the neutralization ability of interest antibodies or their combinations. Antibodies were incubated with the virus for 30 min at

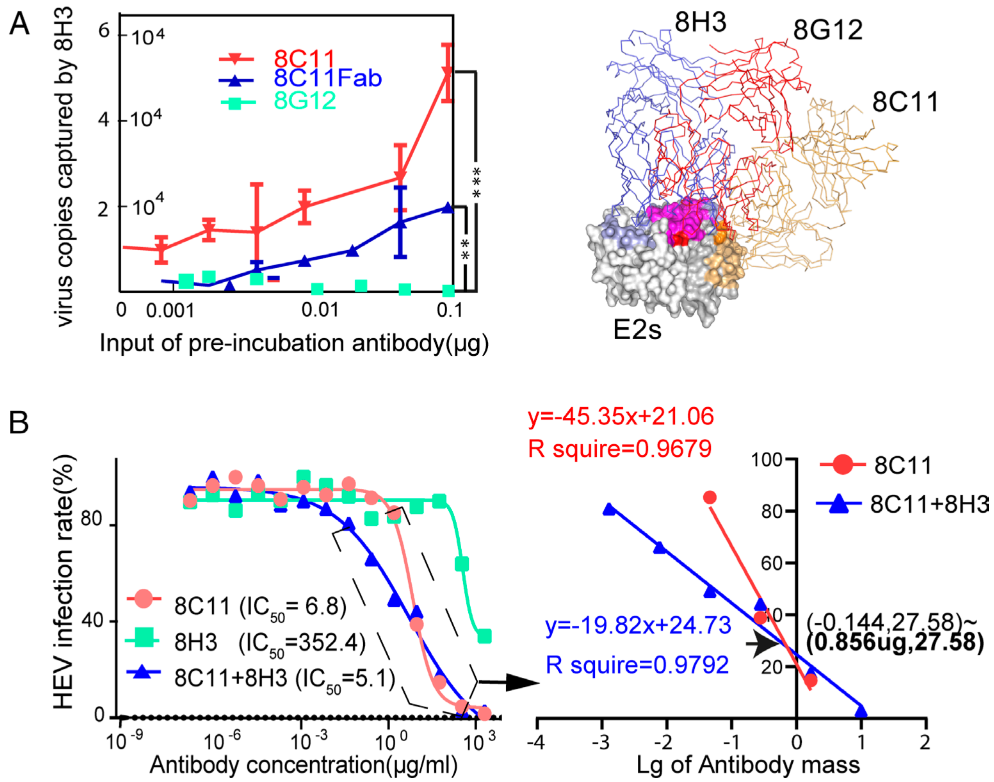

Fig. 7. Coneutralization of 8C11 and 8H3 on Authentic HEV. (*A*) *Left* panel: Red, blue, and green lines represent the virus capture curve of the virus preincubated with 8C11,8C11 Fab and 8G12 nAbs, respectively. The graph shows the interaction between 8C11 and 8H3 in virus captured by 8H3 on the wells. *Right* panel: Fitting of the crystal structure of the E2s:8C11:8H3 complex. The interacting areas from 8G12, 8H3:8G12, 8H3, 8G12:8C11, and 8C11 are highlighted in red, pink, gray, orange, and light yellow, respectively. (*B*) *Left* panel: the synergistic effect of 8C11 and 8H3 in HEV neutralization. Neutralizing curves of 8C11 and 8H3 alone and in combination. *Right* panel: Dose-dependent neutralizing activity of 8C11, 8H3, and their optimal combination dosage evaluated by fitting in simple linear regression. The junction indicates optimal dosage.

37 °C before HepG2/C3A cell inoculation. For the 8C11 and 8H3 group, 8C11 was incubated with the virus for 30 min at 37 °C first, followed by the addition of 8H3 and incubation for another 30 min at 37 °C. Dosage was a sixfold dilution. After 6 h, the inoculum was removed, cells were washed three times with PBS, followed by incubation with DMEM supplemented with 10% FBS and 2% DMSO for 5 d. $ORF2^S$ in cell culture supernatant was checked by ELISA using the HEV detection Kit (Innovax, InnoDx). $ORF2^S$ amount showed a positive correlation to virus. Data were analyzed by GraphPad (GraphPad Prism, Inc.). The synergistic and antagonistic effects between 8C11 and 8H3 or virus neutralization were evaluated by the median effect analysis method with the CompuSyn software (ComboSyn Inc.). This approach determines the dose-dependent neutralization efficacy by each antibody alone and in combination. The constant ratio was set at 1:1, as well as the mixture rate, Fa = 0.9. Virus (Kernow c1 p6, HEV-III) was prepared using S10-3 cells.

Structure Preprocessing. The structures of E2s:8H3 and E2s:8C11 complexes were derived from the cocrystal structure of the E2s:8H3:8C11 complex, respectively, with only one Fab preserved. The model of E2s-I529A mutant was generated using ChimeraX software.

Simulation System Setup. The Autopsf plugin in the Visual Molecular Dynamics software (VMD, version 1.9.3) (36) was used to generate a dynamics-ready protein atom coordinate file (PDB) and a protein structure file. The prepared structure was submitted to Autopsf with the default settings and the CHARMM36 force field topology files. The structure was then embedded in an explicit solvent(water) box, encompassing 12 Å from the protein boundary, using the TIP3P water potential model (37). The system was neutralized by adding counter-chloride ions to achieve a zero charge, followed by additional sodium and chloride ions to a final physiological concentration of 0.15 M.

MD Simulation. MD simulations were performed using the Nanoscale molecular dynamics (NAMD) version 2.14 MD package (38) Compiled with Compute unified device architecture (CUDA) support on an InfiniBand-based cluster. We employed the CHARMM36 force field in our simulations and periodic boundary conditions were used to avoid edge effects. Prior to the production run, the systems were energy-minimized by performing 2,000 conjugate gradient steps to reduce steric conflicts between water molecules and the protein. The energy-minimized structures were then gradually heated to 310 K and equilibrated under this temperature for 100 ps. The equilibrations were conducted under the isothermal-isochoric (NVT) (constant temperature, constant volume) ensemble conditions, with the backbone beads of the protein being fixed. Finally, the equilibrated systems were simulated for 200 ns under the isothermal-isobaric (NPT) (constant temperature, constant pressure) ensemble conditions, and coordinates were saved every 4 ps for analysis.

MD Result Analysis. The Cα RMSF values of both antibodies and E2s domain were calculated using the VMD program with respect to the initial structure of the E2s domain. To calculate the binding free energy of 8H3 with the E2s domain and the E2s:8C11 complex, we used the MM-PBSA (Molecular Mechanics Poisson–Boltzmann Surface Area) method. The MM-PBSA calculations for each complex were carried out using the MMPBSA.py program in AmberTools (39).

Negative-Staining EM. The purified HEV VLP and immune complexes were diluted in PBS (pH 7.4) and then absorbed onto 200 mesh carbon-coated copper grids (Quantifoil Micro Tools) for 90 s then negatively stained with 1.6% phosphotungstic acid (pH 6.4) for 30 s. Specimens were evaluated and imaged with the FEI Tecnai T12 TEM at 150,000× magnification.

Dosage-Dependent Neutralizing Activity and Optimal Dosage Prediction. Dose-dependent neutralizing activity of 8C11, 8H3, and their optimal combination dosage was evaluated by GraphPad. Data within the linearity range were fitted using simple linear regression, generating a predicted optimal dosage. Dose-dependent neutralizing activity of 8C11, 8H3, and their optimal combination dosage was evaluated by GraphPad.

Data, Materials, and Software Availability. The coordinates and structure factors for both 8H3Fab and the E2s:8C11Fab:8H3Fab complex have been deposited in the Protein Data Bank [accession nos. 9IY0 (40) and 9IY2 (41)].

ACKNOWLEDGMENTS. We thank the Shanghai Synchrotron Radiation Facility for their assistance with X-ray diffraction. We acknowledge funding support from the Chinese government: National Key Research and Development Program of China (Grant No. 2021YFC2301404), National Natural Science Foundation of China (Grant Nos. 81991491, 32370160, and 82171746), the Natural Science Foundation of Fujian Province (Grant No. 2022J02005), the Science and Technology Major Project of the Ministry of Xiamen (Grant No. 3502Z20203023), and the Natural Science Foundation of Xiamen (Grant No. 3502Z20227165). We acknowledge the language proofreading support provided by ChatGPT 4 in the preparation of this manuscript.

Author affiliations: [a]State Key Laboratory of Vaccines for Infectious Diseases, Xiang An Biomedicine Laboratory, Department of Laboratory Medicine, School of Public Health, School of Life Sciences, Xiamen University, Xiamen 361102, China; and [b]National Institute of Diagnostics and Vaccine Development in Infectious Diseases, State Key Laboratory of Molecular Vaccinology and Molecular Diagnostics, Collaborative Innovation Center of Biologic Products, Xiamen University, Xiamen 361102, China

Author contributions: M.Z., L.Z., X.Z., K.W., Z.Z., J.Z., H.Y., S.L., Y.G., and N.X. designed research; M.Z., L.Z., Z.Y., C.Y., D.Y., H.W., Z.C., S.W., K.Y., and Y.L. performed research; Y.H., Z.Y., Y.C., D.Y., C.L., and Z.T. contributed new reagents/analytic tools; M.Z., L.Z., Y.H., C.Y., K.W., T.L., Q.Z., Z.Z., J.Z., H.Y., S.L., Y.G., and N.X. analyzed data; and M.Z., L.Z., Y.H., S.L., Y.G., and N.X. wrote the paper.

1. A. Goel, R. Aggarwal, Hepatitis E: Epidemiology, clinical course, prevention, and treatment. *Gastroenterol. Clin. North Am.* **49**, 315–330 (2020).
2. H. R. Dalton, N. Kamar, J. Izopet, Hepatitis E in developed countries: Current status and future perspectives. *Future Microbiol.* **9**, 1361–1372 (2014).
3. E. Tsega, B. G. Hansson, K. Krawczynski, E. Nordenfelt, Acute sporadic viral hepatitis in Ethiopia: Causes, risk factors, and effects on pregnancy. *Clin. Infect. Dis.* **14**, 961–965 (1992).
4. G. H. Lee *et al.*, Chronic infection with camelid hepatitis E virus in a liver transplant recipient who regularly consumes camel meat and milk. *Gastroenterology* **150**, 355–357.e3 (2016).
5. N. Kamar *et al.*, Factors associated with chronic hepatitis in patients with hepatitis E virus infection who have received solid organ transplants. *Gastroenterology* **140**, 1481–1489 (2011).
6. R. Gérolami, V. Moal, P. Colson, Chronic hepatitis E with cirrhosis in a kidney-transplant recipient. *N. Engl. J. Med.* **358**, 859–860 (2008).
7. R. B. Perumpail *et al.*, Fatal accelerated cirrhosis after imported HEV genotype 4 infection. *Emerg. Infect. Dis.* **21**, 1679–1681 (2015).
8. N. Kamar *et al.*, Ribavirin for chronic hepatitis E virus infection in transplant recipients. *N. Engl. J. Med.* **370**, 1111–1120 (2014).
9. A. A. van der Eijk, S. D. Pas, R. A. de Man, Hepatitis E virus: A potential threat for patients with liver disease and liver transplantation. *Best Pract. Res. Clin. Gastroenterol.* **31**, 143–150 (2017).
10. C. C. Huang *et al.*, Molecular cloning and sequencing of the Mexico isolate of hepatitis E virus (HEV). *Virology* **191**, 550–558 (1992).
11. J. Meng *et al.*, Primary structure of open reading frame 2 and 3 of the hepatitis E virus isolated from Morocco. *J. Med. Virol.* **57**, 126–133 (1999).
12. Anonymous, Full-length sequence of genotype 3 hepatitis E virus derived from a pig in Thailand. *J. Med. Virol.* **81**, 657–664 (2010).
13. A. W. Tam *et al.*, Hepatitis E virus (HEV): Molecular cloning and sequencing of the full-length viral genome. *Virology* **185**, 120–131 (1991).
14. F. C. Zhu *et al.*, Efficacy and safety of a recombinant hepatitis E vaccine in healthy adults: A large-scale, randomised, double-blind placebo-controlled, phase 3 trial. *Lancet* **376**, 895–902 (2010).
15. J. Zhang *et al.*, Long-term efficacy of a hepatitis E vaccine. *N. Engl. J. Med.* **372**, 914–922 (2015).
16. S. Li *et al.*, Dimerization of hepatitis E virus capsid protein E2s domain is essential for virus-host interaction. *PLoS pathog.* **5**, e1000537 (2009).
17. Y. Debing, D. Moradpour, J. Neyts, J. Gouttenoire, Update on hepatitis E virology: Implications for clinical practice. *J. Hepatol.* **65**, 200–212 (2016).
18. S. Kumar, S. Subhadra, B. Singh, B. K. Panda, Hepatitis E virus: The current scenario. *Int. J. Infect. Dis.* **17**, e228–e233 (2013).
19. X. Yin *et al.*, Origin, antigenicity, and function of a secreted form of ORF2 in hepatitis E virus infection. *Proc. Natl. Acad. Sci. U.S.A.* **115**, 4773–4778 (2018).
20. D. Ying *et al.* Urine is a viral antigen reservoir in hepatitis E virus infection. *Hepatology* **77**, 1722-1734 (2023).
21. J. Zhang *et al.*, Analysis of hepatitis E virus neutralization sites using monoclonal antibodies directed against a virus capsid protein. *Vaccine* **23**, 2881–2892 (2005).
22. X. Tang *et al.*, Structural basis for the neutralization and genotype specificity of hepatitis E virus. *Proc. Natl. Acad. Sci. U.S.A.* **108**, 10266–10271 (2011).
23. Y. Gu *et al.*, Structural basis for the neutralization of hepatitis E virus by a cross-Genotype antibody. *Cell Res.* **25**, 604–620 (2015).
24. Q. Zheng *et al.*, Viral neutralization by antibody-imposed physical disruption. *Proc. Natl. Acad. Sci. U.S.A.* **116**, 26933–26940 (2019).
25. L. Jiang *et al.*, Potent neutralization of MERS-CoV by human neutralizing monoclonal antibodies to the viral spike glycoprotein. *Sci. Trans. Med.* **6**, 234ra259 (2014).
26. E. Giang *et al.*, Human broadly neutralizing antibodies to the envelope glycoprotein complex of hepatitis C virus. *Proc. Natl. Acad. Sci. U.S.A.* **109**, 6205–6210 (2012).
27. T. L. Meister *et al.*, A ribavirin-induced ORF2 single-nucleotide variant produces defective hepatitis E virus particles with immune decoy function. *Proc. Natl. Acad. Sci. U.S.A.* **119**, e2202653119 (2022).
28. C. Montpellier *et al.*, Hepatitis E virus lifecycle and identification of 3 forms of the ORF2 capsid protein. *Gastroenterology* **154**, 211–223.e8 (2018).
29. Q. Zheng *et al.*, Structural basis for the synergistic neutralization of coxsackievirus B1 by a triple-antibody cocktail. *Cell Host Microbe* **30**, 1279–1294.e76 (2022).
30. Z. Tong *et al.*, Deciphering a reliable synergistic bispecific strategy of rescuing antibodies for SARS-CoV-2 escape variants, including BA.2.86, EG.5.1, and JN.1. *Cell Rep.* **43**, 114338 (2024).
31. Y. Sun *et al.*, Structure-based development of three- and four-antibody cocktails against SARS-CoV-2 via multiple mechanisms. *Cell Res.* **31**, 597–600 (2021).
32. J. Liu *et al.*, PD-1/PD-L1 checkpoint inhibitors in tumor immunotherapy. *Front. pharmacol.* **12**, 731798 (2021).
33. H. Yamaguchi, J. M. Hsu, W. H. Yang, M. C. Hung, Mechanisms regulating PD-L1 expression in cancers and associated opportunities for novel small-molecule therapeutics. *Nat. Rev. Clin. Oncol.* **19**, 287–305 (2022).
34. J. J. Germer *et al.*, Hepatitis E Virus (HEV) detection and quantification by a real-time reverse transcription-pcr assay calibrated to the world health organization standard for HEV RNA. *J. Clin. Microbiol.* **55**, 1478–1487 (2017).
35. X. Yin, C. Ambardekar, Y. Lu, Z. Feng, Distinct entry mechanisms for nonenveloped and quasi-enveloped hepatitis E viruses. *J. Virol.* **90**, 4232–4242 (2016).
36. W. Humphrey, A. Dalke, K. Schulten, VMD: Visual molecular dynamics. *J. Mol. Graph.* **14**, 27–38 (1996).
37. W. L. Jorgensen, J. Chandrasekhar, J. D. Madura, R. W. Impey, M. L. Klein, Comparison of simple potential functions for simulating liquid water. *J. Chem. Phys.* **79**, 926–935 (1983).
38. J. C. Phillips *et al.*, Scalable molecular dynamics on CPU and GPU architectures with NAMD. *J. Chem. Phys.* **153**, 044130 (2020).
39. B. R. Miller, *et al.*, MMPBSA.py: An efficient program for end-state free energy calculations. *J. Chem. Theor. Comput.* **8**, 3314–3321 (2012).
40. Z. Minghua, Z. Lizhi, H. Yang, G. Ying, L. Shaowei, anti-HEV mAb 8H3. Protein Data Bank. https://doi.org/10.2210/pdb9IY0/pdb. Deposited 29 July 2024.
41. Z. Minghua, Z. Lizhi, H. Yang, G. Ying, L. Shaowei, Immune complex of HEV-E2s, nAb 8C11 and nAb 8H3. Protein Data Bank. https://doi.org/10.2210/pdb9IY2/pdb. Deposited 29 July 2024.